Article

An optoelectronic synapse based on α-In$_2$Se$_3$ with controllable temporal dynamics for multimode and multiscale reservoir computing

In the format provided by the authors and unedited

An optoelectronic synapse based on α-In$_2$Se$_3$ with controllable temporal dynamics for multimode and multiscale reservoir computing

Keqin Liu[1], Teng Zhang[1], Bingjie Dang[1], Lin Bao[1], Liying Xu[1], Caidie Cheng[1], Zhen Yang[1],

Ru Huang[1,2,3*] & Yuchao Yang[1,2,3,4*]

[1]*Beijing Advanced Innovation Center for Integrated Circuits, School of Integrated Circuits, Peking University, Beijing 100871, China.*

[2]*Center for Brain Inspired Chips, Institute for Artificial Intelligence, Frontiers Science Center for Nano-optoelectronics, Peking University, Beijing 100871, China.*

[3]*Center for Brain Inspired Intelligence, Chinese Institute for Brain Research (CIBR), Beijing, Beijing 102206, China.*

[4]*Beijing Academy of Artificial Intelligence, Beijing 100084, China.*

*Correspondence should be addressed to: yuchaoyang@pku.edu.cn; ruhuang@pku.edu.cn
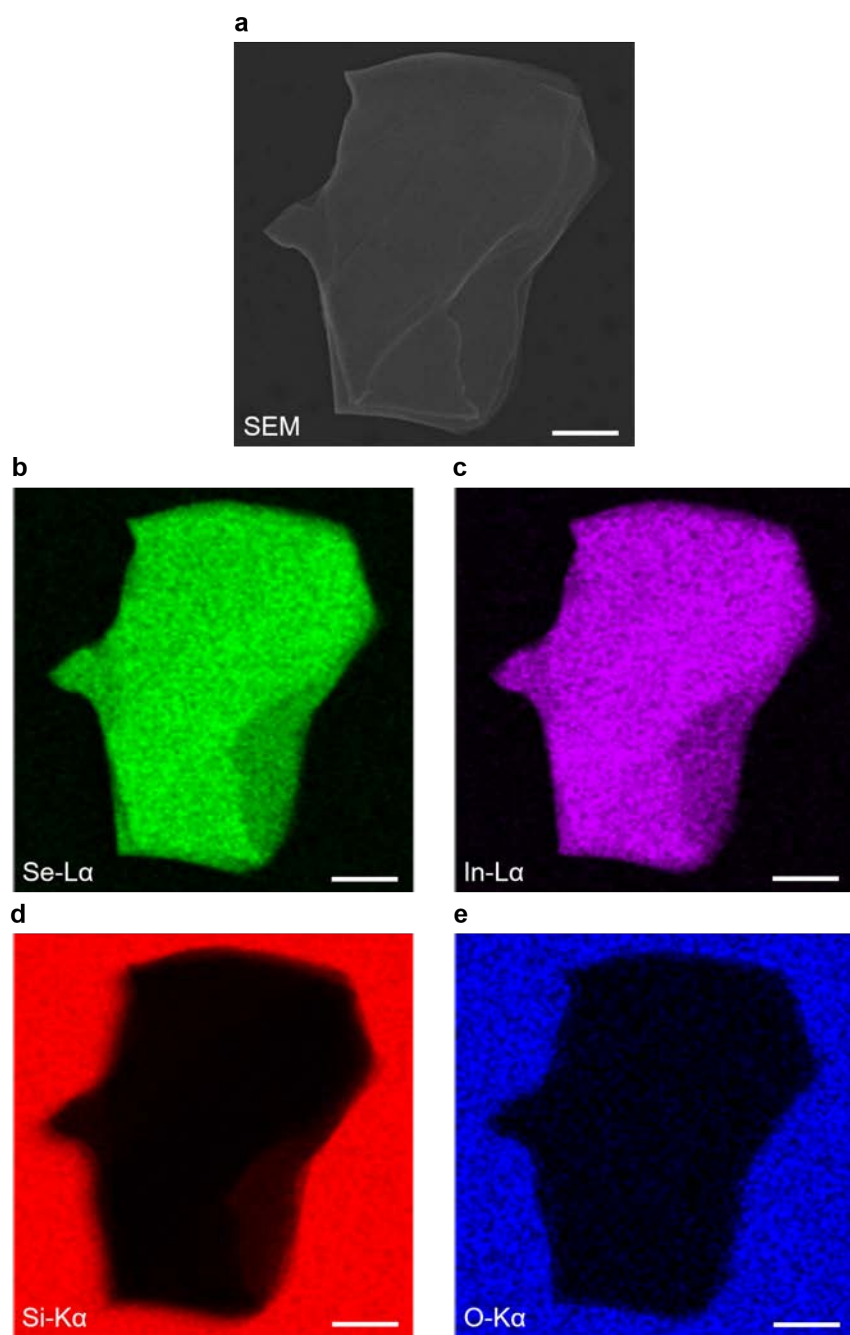
Supplementary Figure 1 | Elemental characterization of a ferroelectric α-In₂Se₃ flake through SEM and EDS mapping. (**a**) Scanning electron microscopy (SEM) image and corresponding (**b-e**) Energy-dispersive X-ray spectroscopy (EDS) mapping of Se L, In L, Si K and O K edges of a ferroelectric α-In$_2$Se$_3$ flake transferred on SiO$_2$ substrate, confirming the elemental composition. Scale bar, 10 μm.
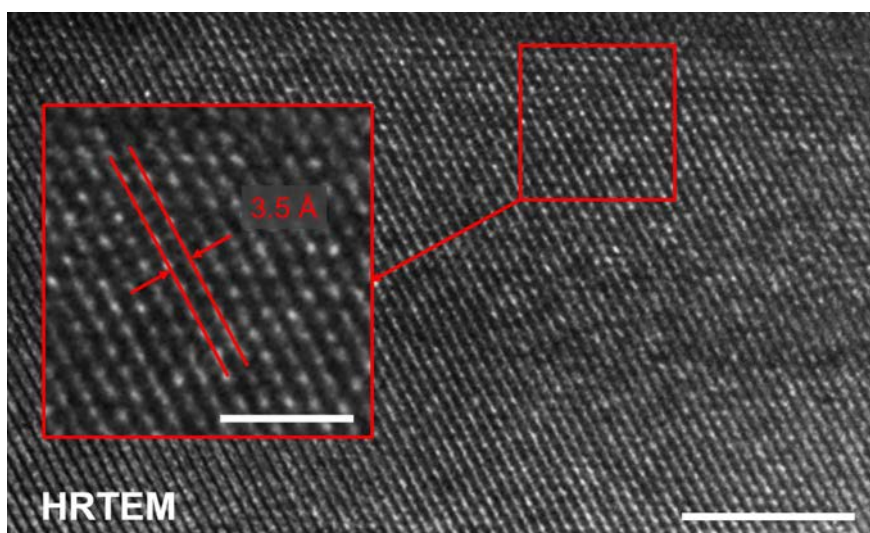
Supplementary Figure 2 | Top-view high-resolution TEM (HRTEM) image of the α-In$_2$Se$_3$ flake, exhibiting highly crystallized structure. Scale bar, 5 nm. Inset shows the magnified image and d-spacing of the plane family is 3.5 Å, in good agreement with the lattice constant of (100) lattice plane of α-In$_2$Se$_3$. Scale bar, 2 nm.
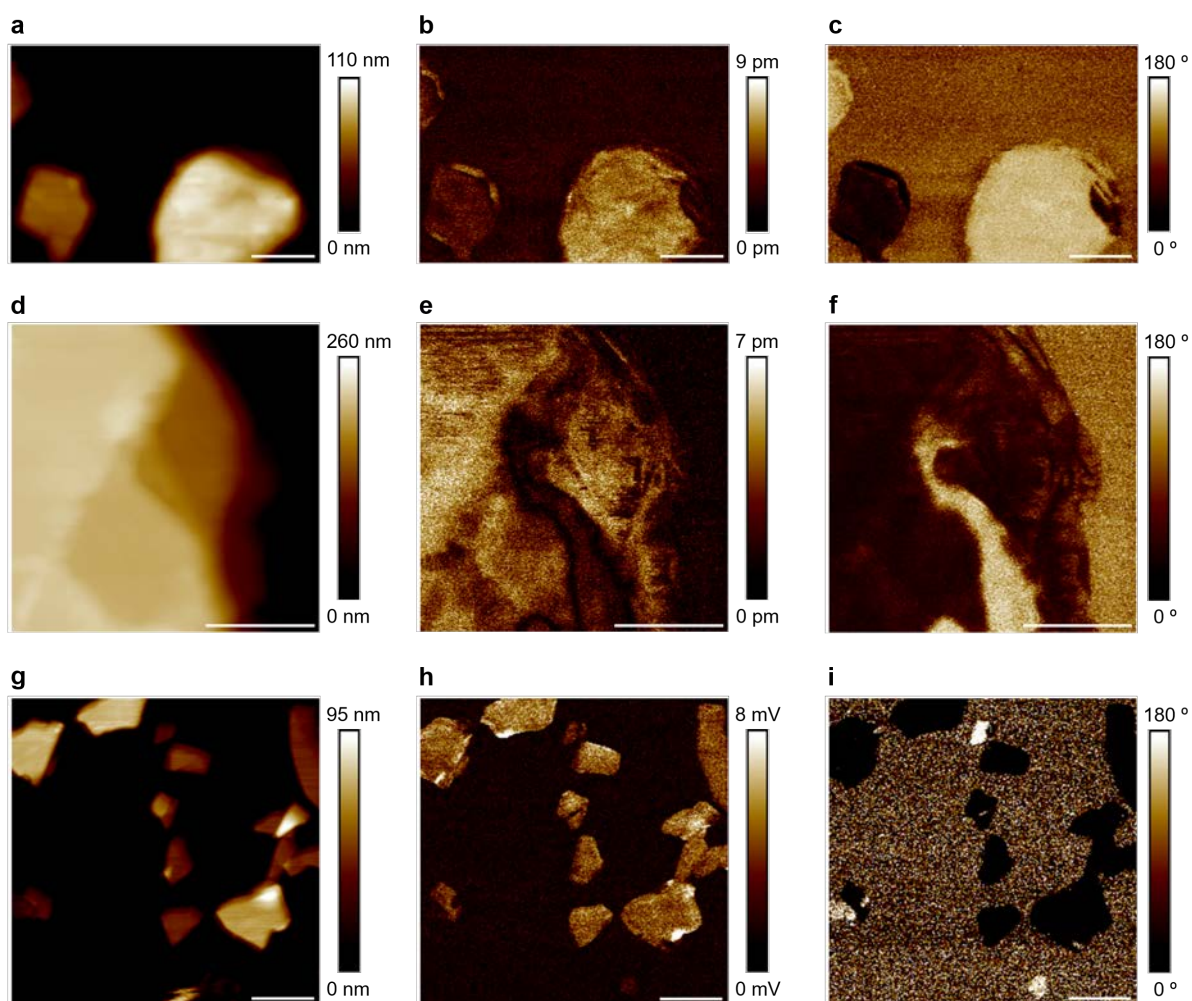
Supplementary Figure 3 | Characterization of ferroelectric α-In₂Se₃ flakes through piezoresponse force microscopy. (a-f) Topography (**a, d**), out-of-plane PFM amplitude (**b, e**) and out-of-plane PFM phase (**c, f**) images of α-In₂Se₃ flakes acquired at contact resonance, exhibiting opposite phase among flakes as well as opposite phase between different domain regions separated by domain walls in one flake. Scale bar: 800 nm. **(g-i)** Topography (**g**), out-of-plane PFM amplitude (**h**) and out-of-plane PFM phase (**i**) acquired at non-contact resonance, where a tip with stiff cantilever (80 N/m) was used to eliminate the electrostatic contribution. Scale bar: 2 μm.
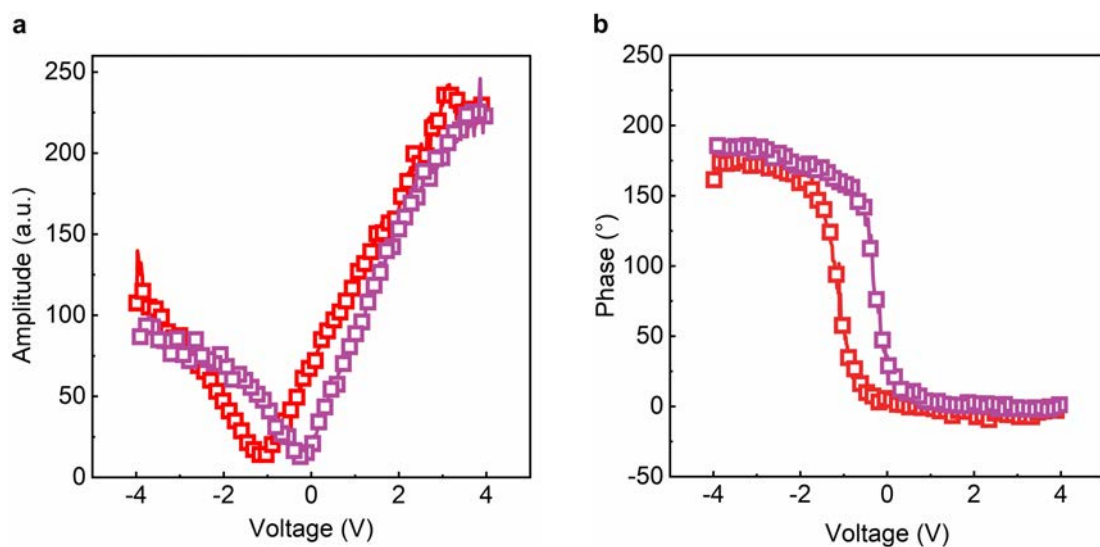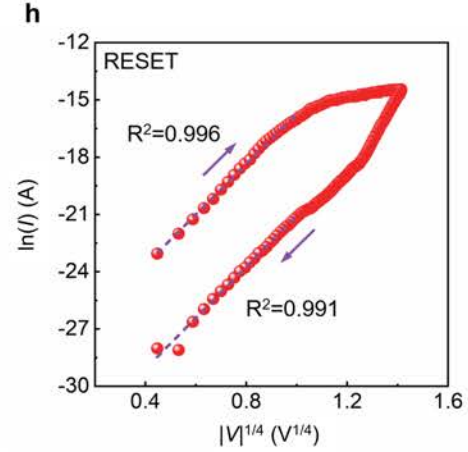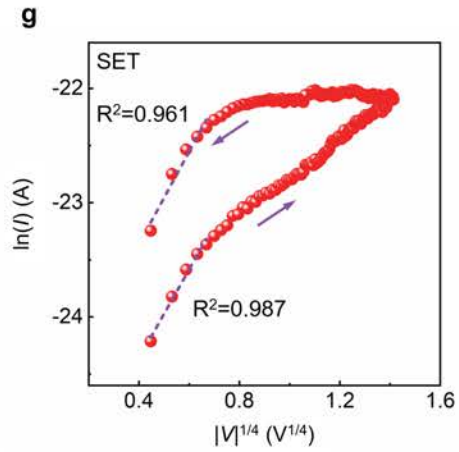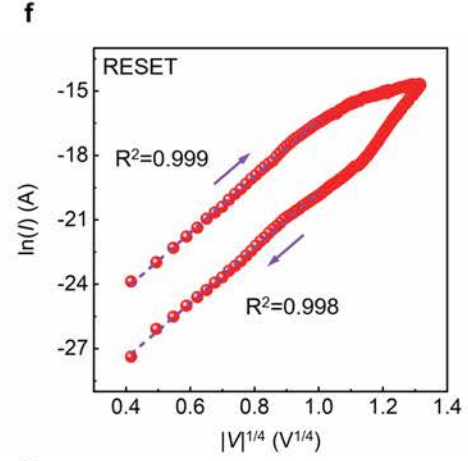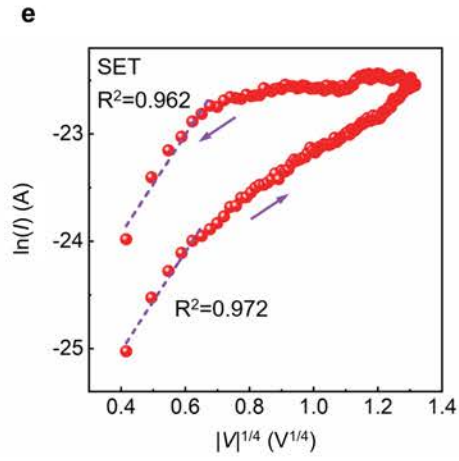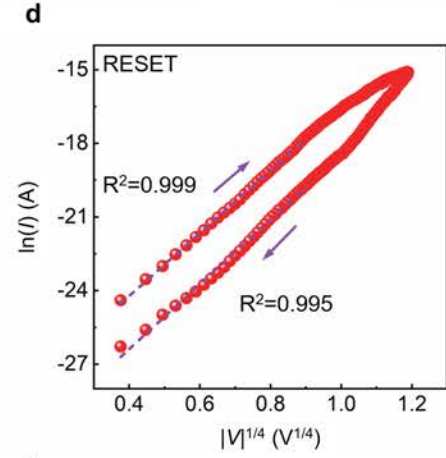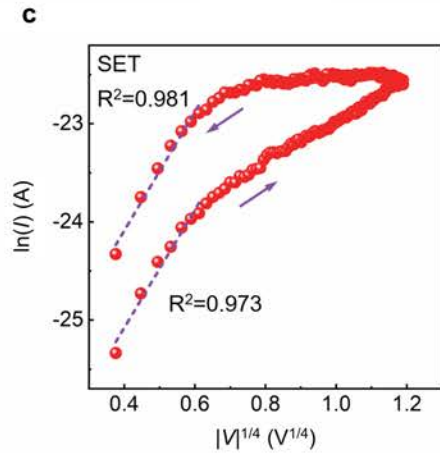
Supplementary Figure 4 | Switching spectroscopy PFM performed on α-In$_2$Se$_3$ flakes. (a) PFM amplitude shows a typical butterfly loop. (**b**) PFM phase contrast of 180° is clearly observed. These results show the ferroelectric polarization switching under external electric field.

Supplementary Table 1 | Summary of the presence of Raman Peak at ~89 cm^{-1} for 2H and 3R α-In$_2$Se$_3$.

Reference	Crystal Structure	TEM	Raman Peak at ~89 cm^{-1}
This work	3R α-In$_2$Se$_3$	Y	Y
Ref. S1	3R α-In$_2$Se$_3$	Y	Y
Ref. S2	3R α-In$_2$Se$_3$	Y	Y
Ref. S3	3R α-In$_2$Se$_3$	Y	Y
	2H α-In$_2$Se$_3$	Y	Y
Ref. S4	2H α-In$_2$Se$_3$	Y	Y
Ref. S5	2H α-In$_2$Se$_3$	Y	Y

Supplementary Figure 5 | Transport characteristics of the α-In₂Se₃ device. Plot of $\ln(I)$ as a function of $|V|^{1/4}$ for the SET process in (**a**) 1 V, (**c**) 2 V, (**e**) 3 V, (**g**) 4 V and RESET process in (**b**) -1 V, (**d**) -2 V, (**f**) -3 V, (**h**) -4 V. The good linear fitting is consistent with thermionic field emission model for charge injection.
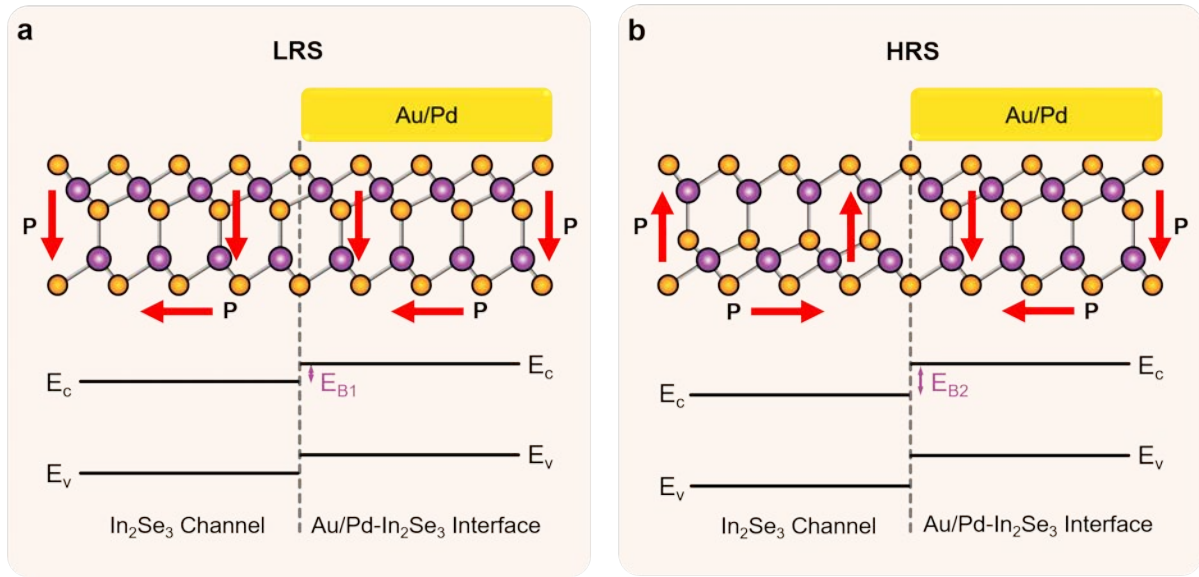
Supplementary Figure 6 | Memristive switching mechanism of the α-In₂Se₃ device. Ferroelectric domain configurations and band alignment between domains of α-In₂Se₃ device in (**a**) low resistance state (LRS) and (**b**) high resistance state (HRS). The energy barrier increases from E_{B1} in LRS to E_{B2} in HRS, leading to rising device resistance.
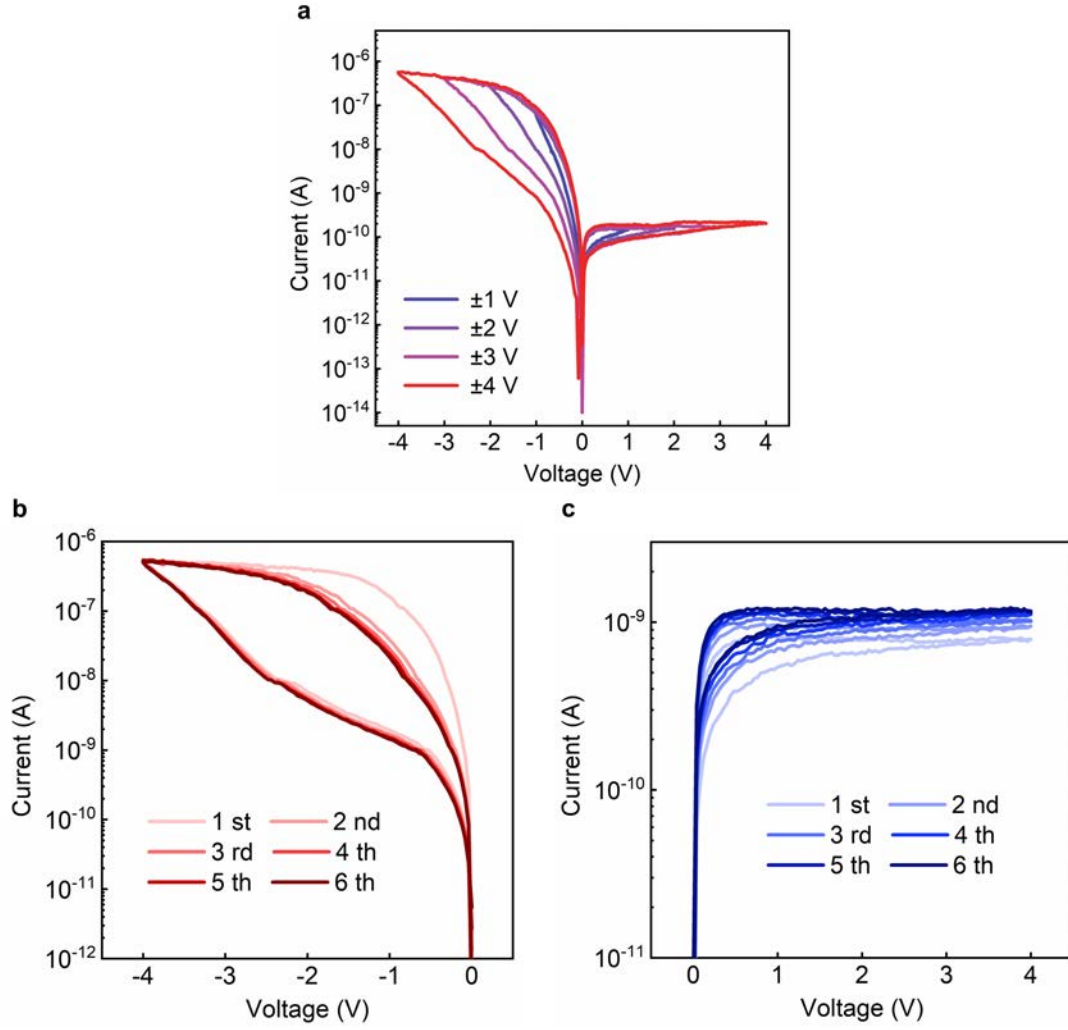
Supplementary Figure 7 | Electrical characterization of ferroelectric α-In$_2$Se$_3$ memristive device. (**a**) DC switching characteristics of α-In$_2$Se$_3$ device with increased SET and RESET voltages from ±1 V to ±4 V, where increased hysteresis can be observed. (**b-c**) Consecutive SET (4 V) or RESET (-4 V) voltage sweep is performed, where the trace of second sweep doesn't follow the retrace of the first sweep exactly, demonstrating the mixture of nonvolatile and volatile resistive switching in α-In$_2$Se$_3$ device.
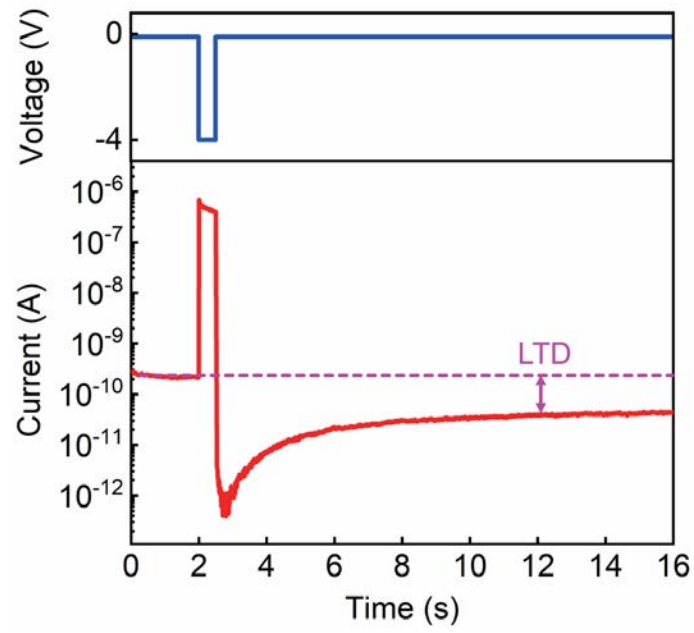
Supplementary Figure 8 | Long-term plasticity in ferroelectric α-In₂Se₃ device. Appling a sufficient large electrical pulse (-4 V, 500 ms), long-term depression effect can be clearly observed.
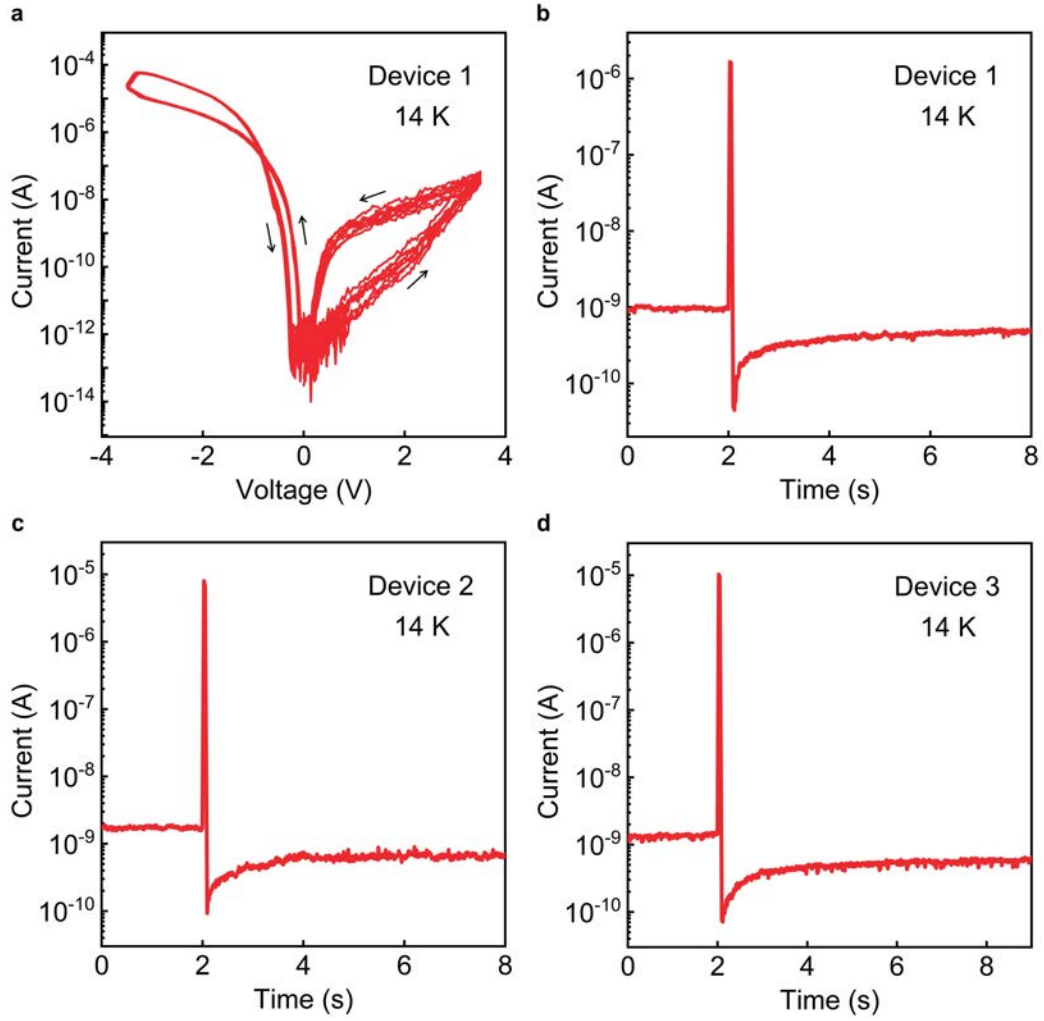
Supplementary Figure 9 | Low temperature measurement of the α-In₂Se₃ device. (**a**) DC characteristics of the α-In₂Se₃ device at 14 K, where SET and RESET processes can still be observed. Since charge trapping/de-trapping process is suppressed at low temperature, the memristive switching behavior can be attributed to ferroelectric polarization switching. (**b-d**) Transient behavior of three different α-In₂Se₃ devices at 14 K, where a negative voltage pulse was applied (-2 V, 50 ms) with -0.5 V bias to read the device state. The transient behavior can still be observed at 14 K, indicating ferroelectric polarization switching may also contribute to this transient behavior.
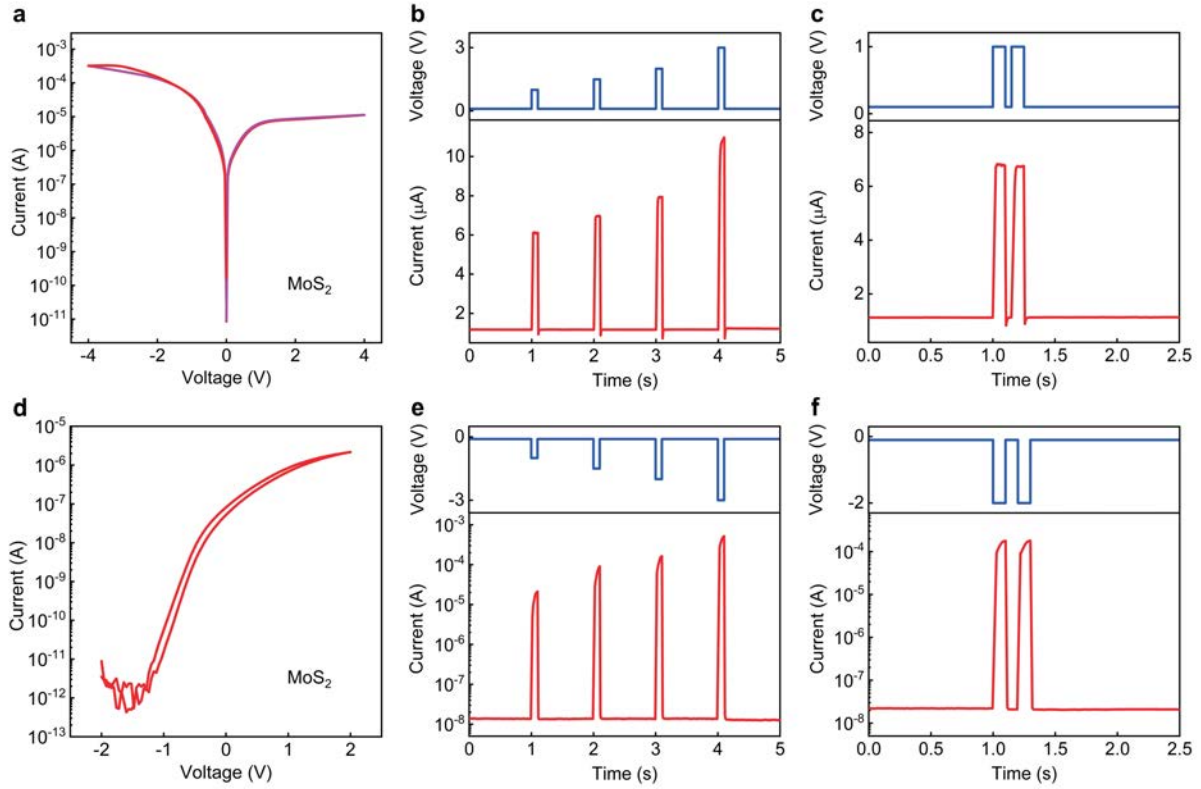
Supplementary Figure 10 | Control experiment of MoS₂ devices fabricated on the HfO₂ substrate. (**a**) DC characteristics of the MoS₂ device (thickness 6 nm) exhibited negligible hysteresis. (**b**) Pulse test with positive electrical pulses (1 V, 1.5 V, 2 V, 3 V, 100 ms pulses) and 0.1 V bias to read the device state, exhibiting negligible transient behaviours. (**c**) Paired-pulse test, where a pair of positive pulses was applied (1 V, 100 ms, with an interval of 50 ms) with 0.1 V bias to read the device state. (**d**) Transfer curve of the MoS₂ device (V_{ds} = 0.1 V) exhibits a small hysteresis, proving that limited number of traps exist in HfO₂ substrate. (**e**) Pulse test with negative electrical pulses (-1 V, -1.5 V, -2 V, -3 V, 100 ms pulses) and -0.1 V bias to read the device state. (**f**) Paired-pulse test, where a pair of negative pulses was applied (-2 V, 100 ms, with an interval of 100 ms) with -0.1 V bias to read the device state.
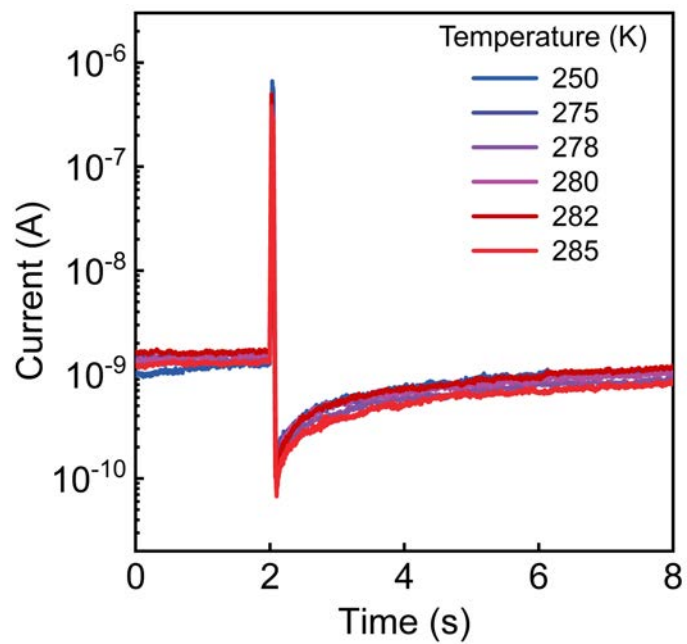
Supplementary Figure 11 | Transient behavior of the α-In₂Se₃ device with slight temperature variations. Consistent transient behavior with slight variations was observed when a voltage pulse was applied (-2V, 50 ms with -0.1 V bias) with temperature varied from 250 K to 285 K.
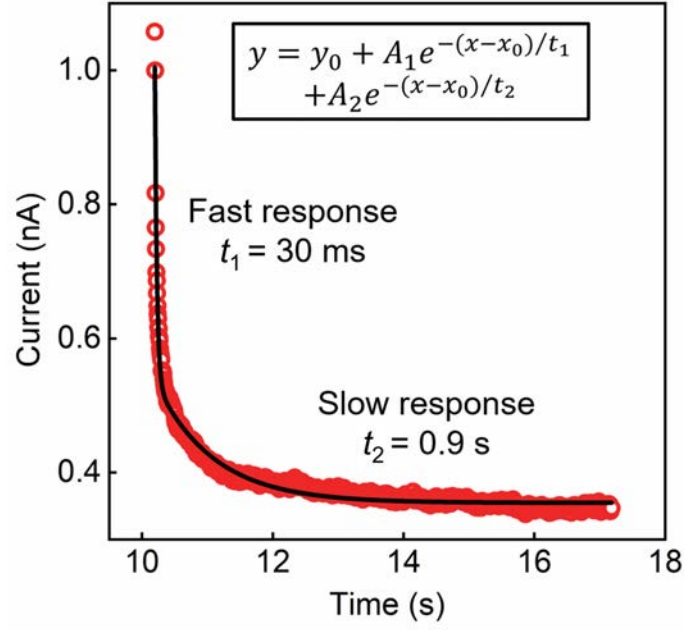
Supplementary Figure 12 | Fitting the photocurrent decay process in α-In₂Se₃ optoelectronic synapse. The result can be well fitted by a double exponential decay function and two different time constants are obtained. As a result, $t_1 = 30$ ms corresponds to a fast decay process and $t_2 = 0.9$ s corresponds to a slow decay process, indicating two different mechanisms play a role in the photocurrent decay process.
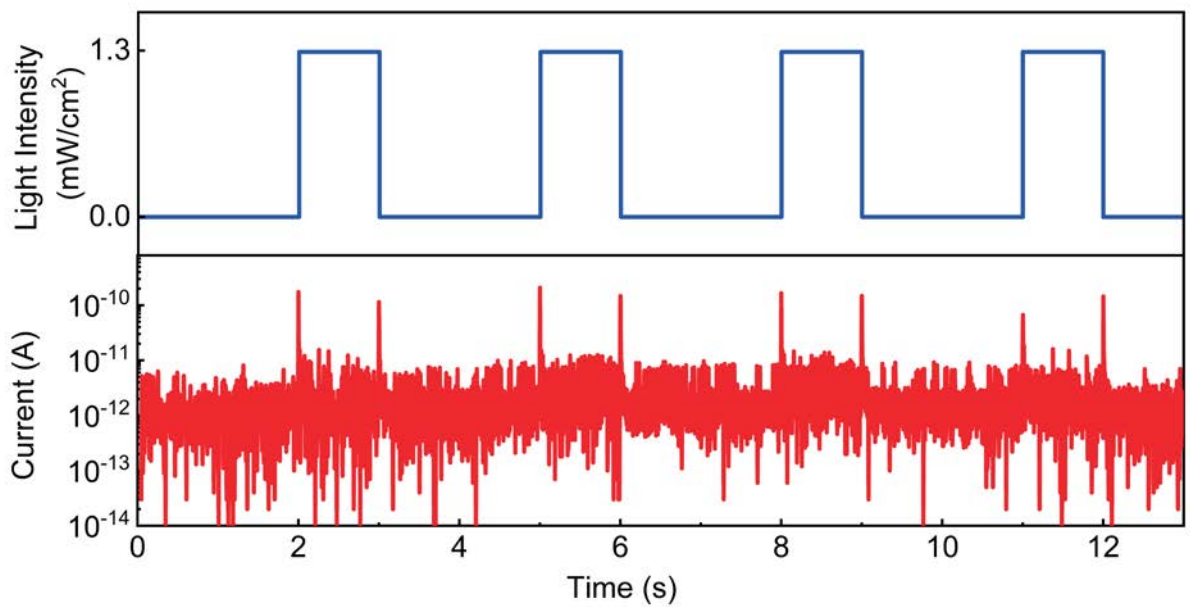
Supplementary Figure 13 | Control experiment to investigate the current contribution of HfO₂/Si interface. Planar devices (source-drain distance of ~1 μm) without α-In₂Se₃ flakes were fabricated on the HfO₂ substrate. Light pulses (1.29 mW/cm², 1 s) were applied to the device with -0.1 V read bias, and negligible current response can be observed.
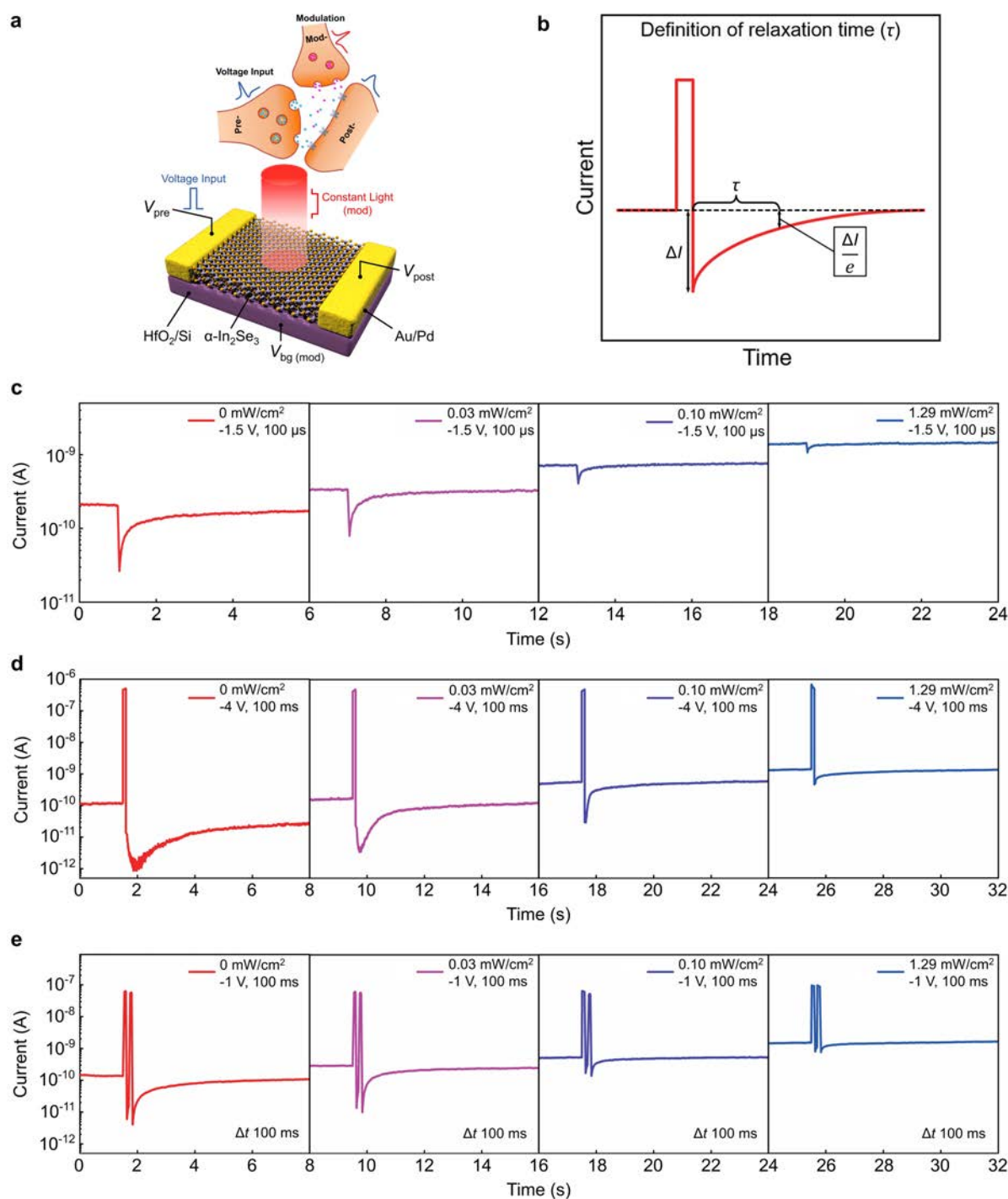
Supplementary Figure 14 | Relaxation time of α-In₂Se₃ device under various electrical stimuli and light intensities. (**a**) Schematic illustration of heterosynaptic plasticity with constant light as the modulation terminal. (**b**) The definition of relaxation time for a typical PSC curve, which is the duration for the inhibition effect (ΔI) to recover to its $1/e$. (**c**) A weak electrical pulse (-1.5 V, 100 μs) was applied to the α-In₂Se₃ device with increased light intensities (0 mW/cm², 0.03 mW/cm², 0.10 mW/cm², 1.29 mW/cm²). The relaxation process and current level are modulated by light intensity. The rising part of PSC was not collected, due to pulse width is below the time resolution limit of the semiconductor analyzer. (**d-e**) Synaptic plasticity modulated by constant light (0 mW/cm², 0.03 mW/cm², 0.10 mW/cm² and 1.29 mW/cm²). An electrical pulse (-4 V, 100 ms) induced LTD is suppressed by light illumination, exhibiting decreased relaxation time and increased current level with higher light intensity. Paired-pulse depression effect, where a pair of electrical pulses was applied (-1 V, 100 ms, with an interval of 100 ms), is weakened by constant light (0 mW/cm², 0.03 mW/cm², 0.10 mW/cm² and 1.29 mW/cm²) because of the shortened relaxation time.
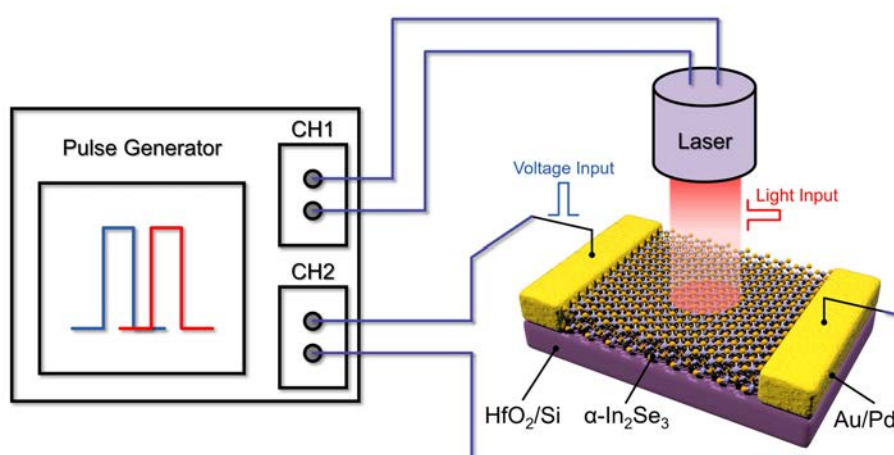
Supplementary Figure 15 | Experimental setup for controlling the timing between voltage and light inputs. The pulse generator generated two voltage pulses with controlled time interval in two different channels (CH1 and CH2). Voltage pulse generated from CH1 was applied to the laser and produced a light input, meanwhile, the voltage pulse from CH2 was directly applied to the device as electrical input. Since the timing of voltage pulses generated from two channels can be accurately controlled by the pulse generator, the timing of light and voltage inputs can therefore be accurately controlled.
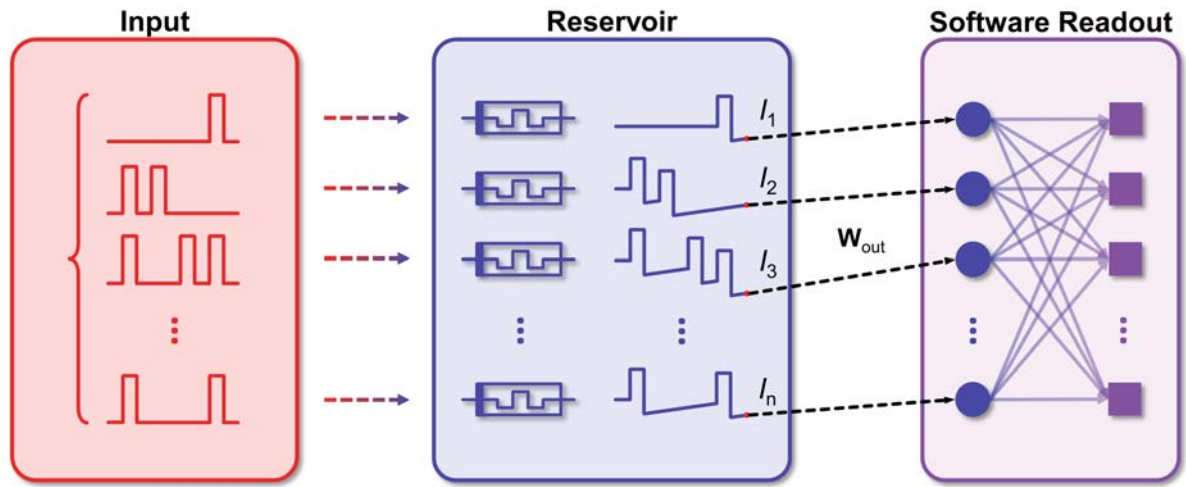
Supplementary Figure 16 | Schematic diagram of the operation of mixed-input reservoir computing. The input image (20×20) was grouped into 4 consecutive pixels and formed a 100×4 input where each row was converted into 4 pulses and applied to the reservoir. The current value was collected after every four pulses and fed into the software readout layer with ten output neurons to calculate the probability of different outputs.
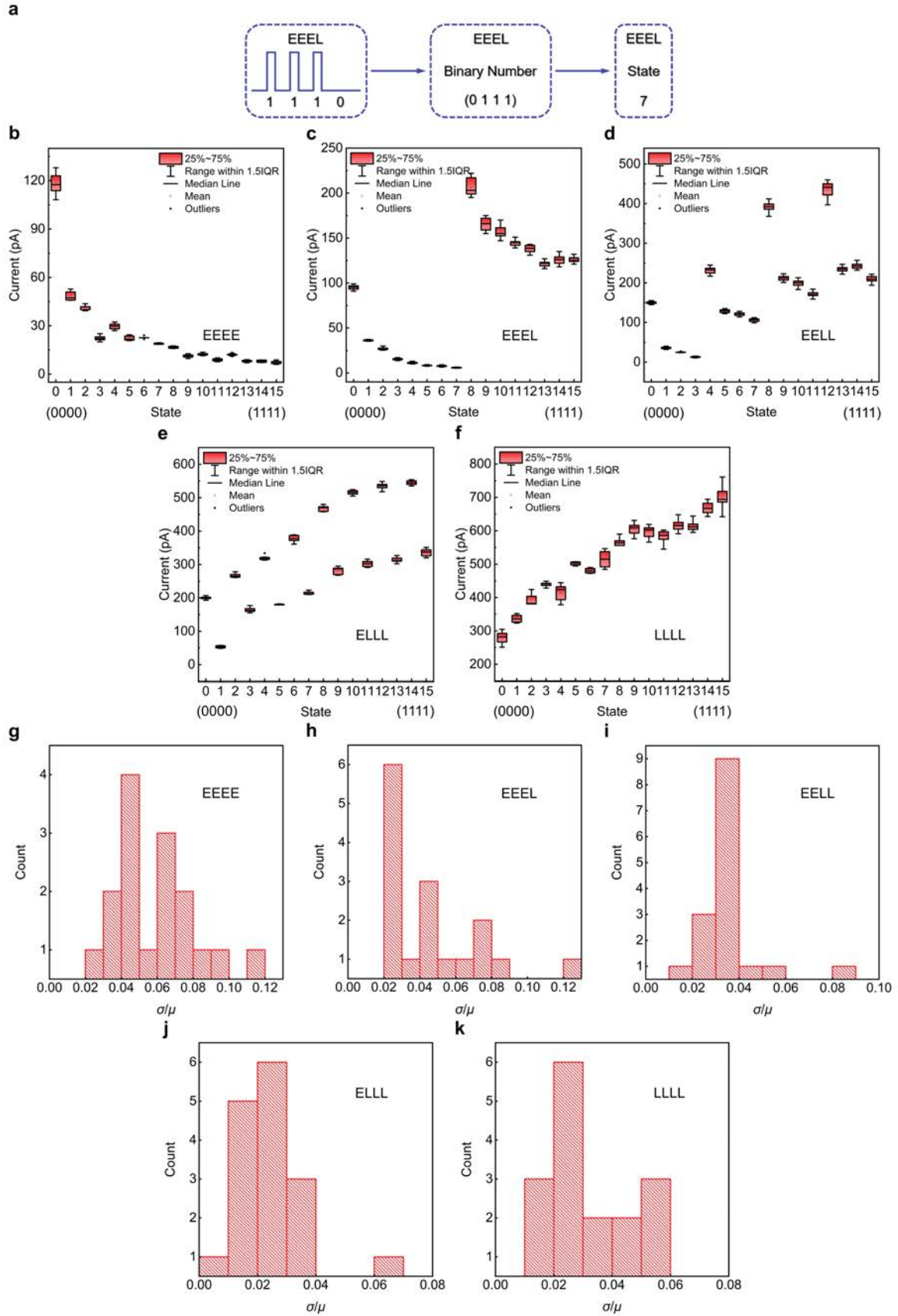
Supplementary Figure 17 | The nonlinear transformation results with various reservoir

modes. (a) Each input waveform corresponds to a reservoir state number, taking "EEEL" as

an example. Then, the readout current is plotted versus state to demonstrate the nonlinear transformation relationships. (**b-f**) Nonlinear transformation results of (**b**) "EEEE", (**c**) "EEEL", (**d**) "EELL", (**e**) "ELLL" and (**f**) "LLLL" demonstrate different reservoir states distribution. Inhomogeneous distribution of reservoir states in "EEEE" can be clearly observed. Through incorporating light input, more even distributions are achieved in "EELL", "EEEL" and "LLLL". Meanwhile, each nonlinear transformation mode possesses a unique mapping order, which may also affect the network performance. Notably, pure light input shows evenly distributed reservoir states, resulting in good performance with accuracy of 97.7% and prospects for in-sensor reservoir computing. (**g-k**) Distribution of coefficient of variation (σ/μ) for different working modes, where the majority of σ/μ is no more than 0.1.
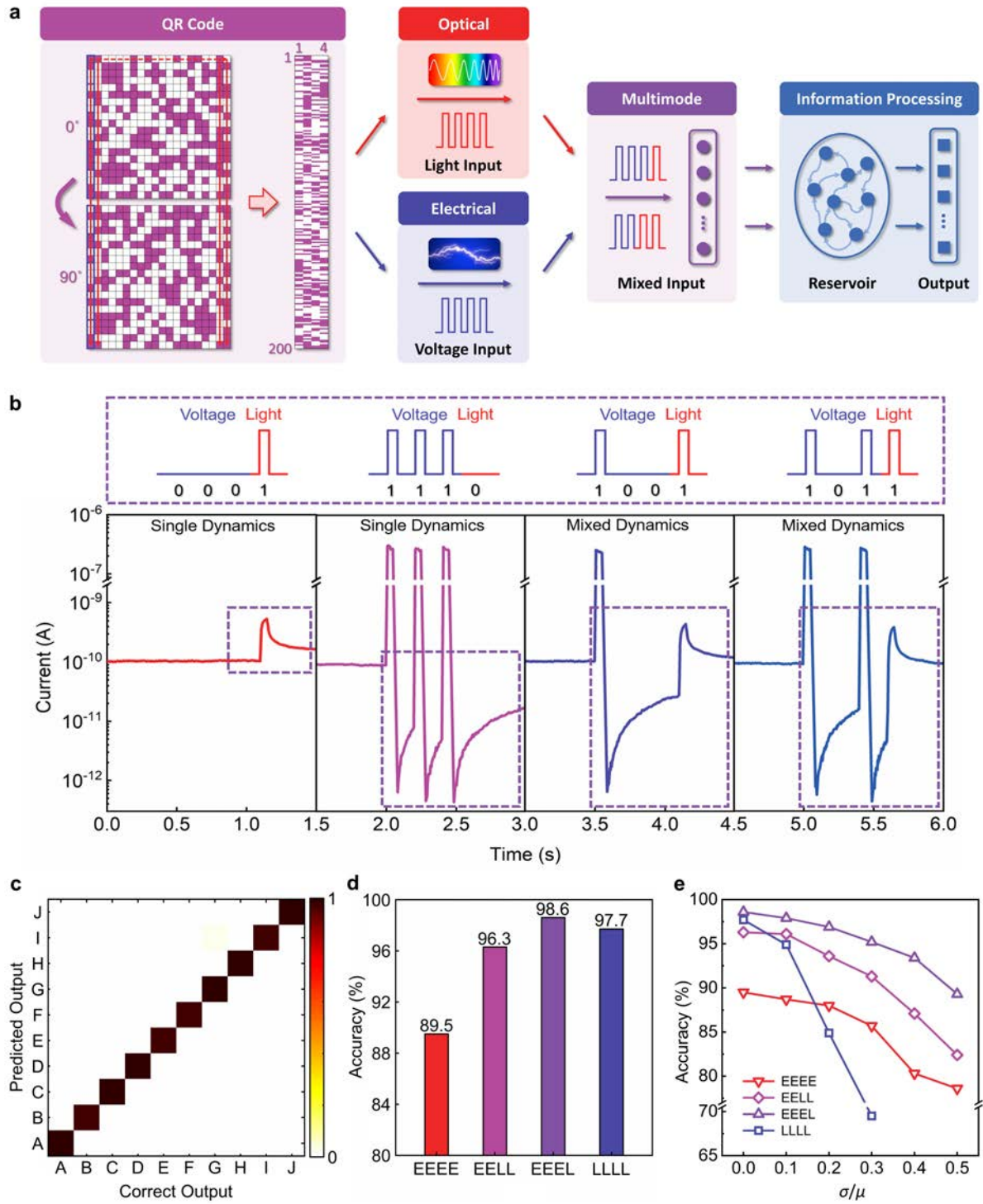
Supplementary Figure 18 | Mixed-input reservoir computing with tunable dynamics. (a)

Schematic of mixed-input reservoir computing for QR code recognition task. QR code (21×21)

was cut (20×20), rotated by 0° and 90°, then combined together (40×20). The pixels were

transformed into pulse trains, where light pulses represent optical input and electrical pulses

represent voltage input. Then signal was mixed with various modes as the input of RC system. Based on the optoelectronic response of α-In$_2$Se$_3$, mixed-signal reservoir computing with tunable nonlinear transformation mode is realized. (**b**) Dynamic response of RC system operated at "EEEL" mode. Light input utilizes optoelectronic dynamics of α-In$_2$Se$_3$, whereas, electrical input utilizes ferroelectric dynamics of α-In$_2$Se$_3$. Moreover, mixed input utilizes both of them and their interactions. (**c**) Confusion matrix showing the experimentally obtained classification results from the RC system operated at "EEEL" mode versus the correct outputs. A recognition accuracy of 98.6% is achieved. (**d**) Recognition accuracies of RC systems operated at different modes ("EEEE", "EELL", "EEEL", "LLLL") are summarized. Recognition accuracy of "LLLL" is higher than "EEEE". Through tuning the nonlinear transformation mode, the performance of "EEEE" can be improved ("EELL") and even optimized ("EEEL") by partially substituting electrical pulses into light pulses. (**e**) The influence of cycle-to-cycle variation (σ/μ) on network performances, where the recognition accuracies for different modes decreased with increased σ/μ.
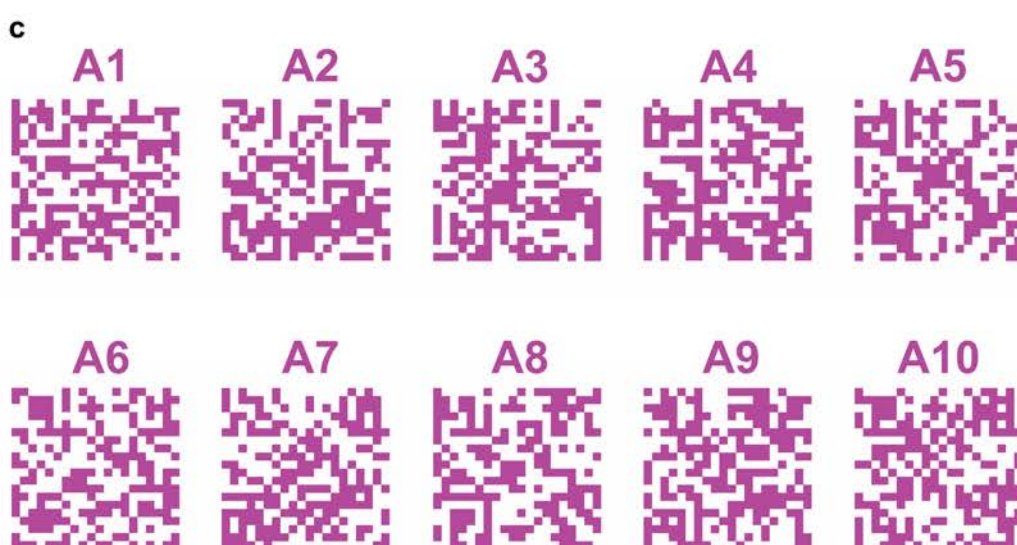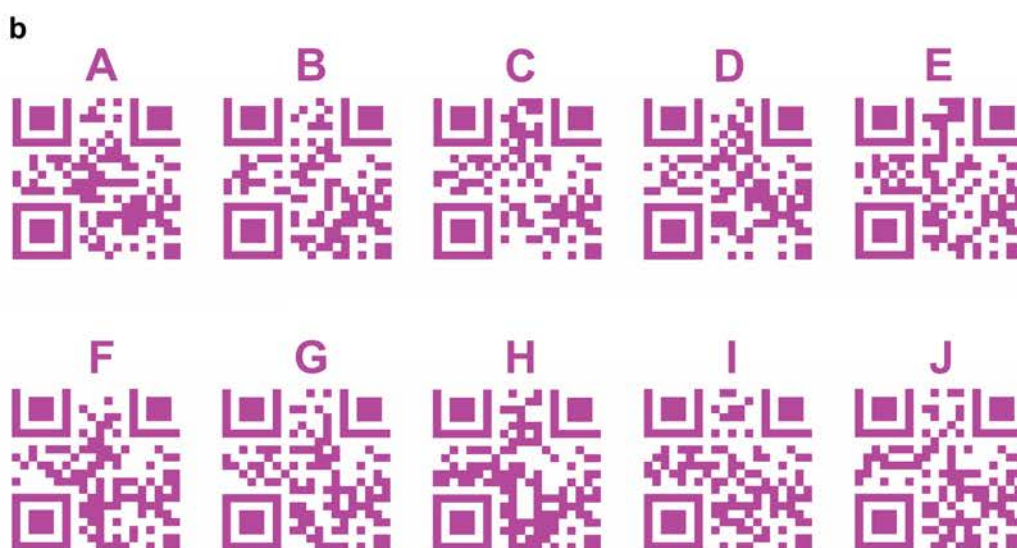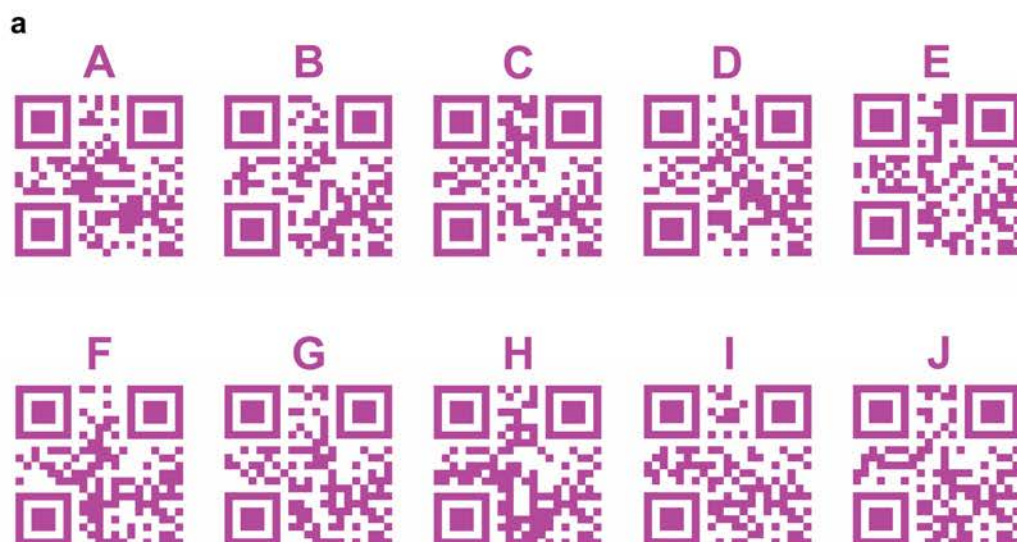
Supplementary Figure 19 | Schematic diagram of QR codes used in the recognition task.

(**a**) QR codes represent ten letters from "A" to "J". Each QR code has a size of 21×21. (**b**) The pixels in the right column and top row of the QR code are cut to form a size of 20×20. (**c**) QR code for each letter is added by 25% noise and 400 instances are generated for each letter. Ten examples of generated noisy QR codes representing letter "A" are shown here.
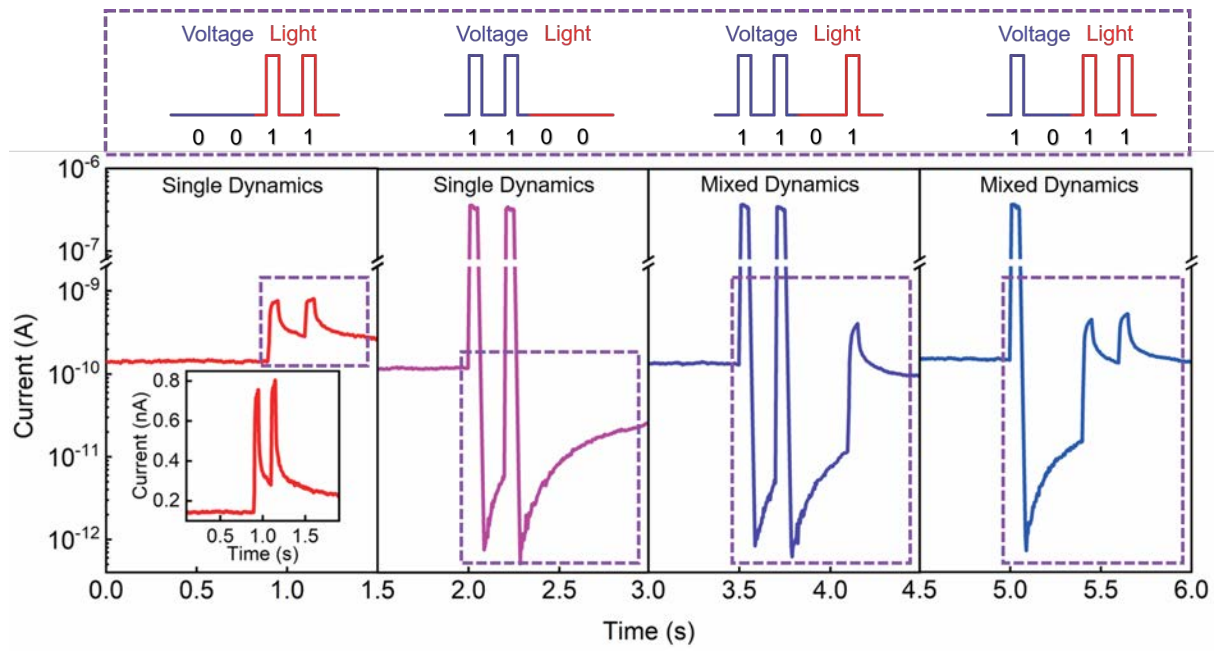
Supplementary Figure 20 | Dynamic response of RC system operated at "EELL" mode. Light input utilizes optoelectronic dynamics of α-In$_2$Se$_3$, whereas, electrical input utilizes ferroelectric dynamics of α-In$_2$Se$_3$. Moreover, mixed input utilizes both of them and their interaction, thus generating a new nonlinear transformation relationship.
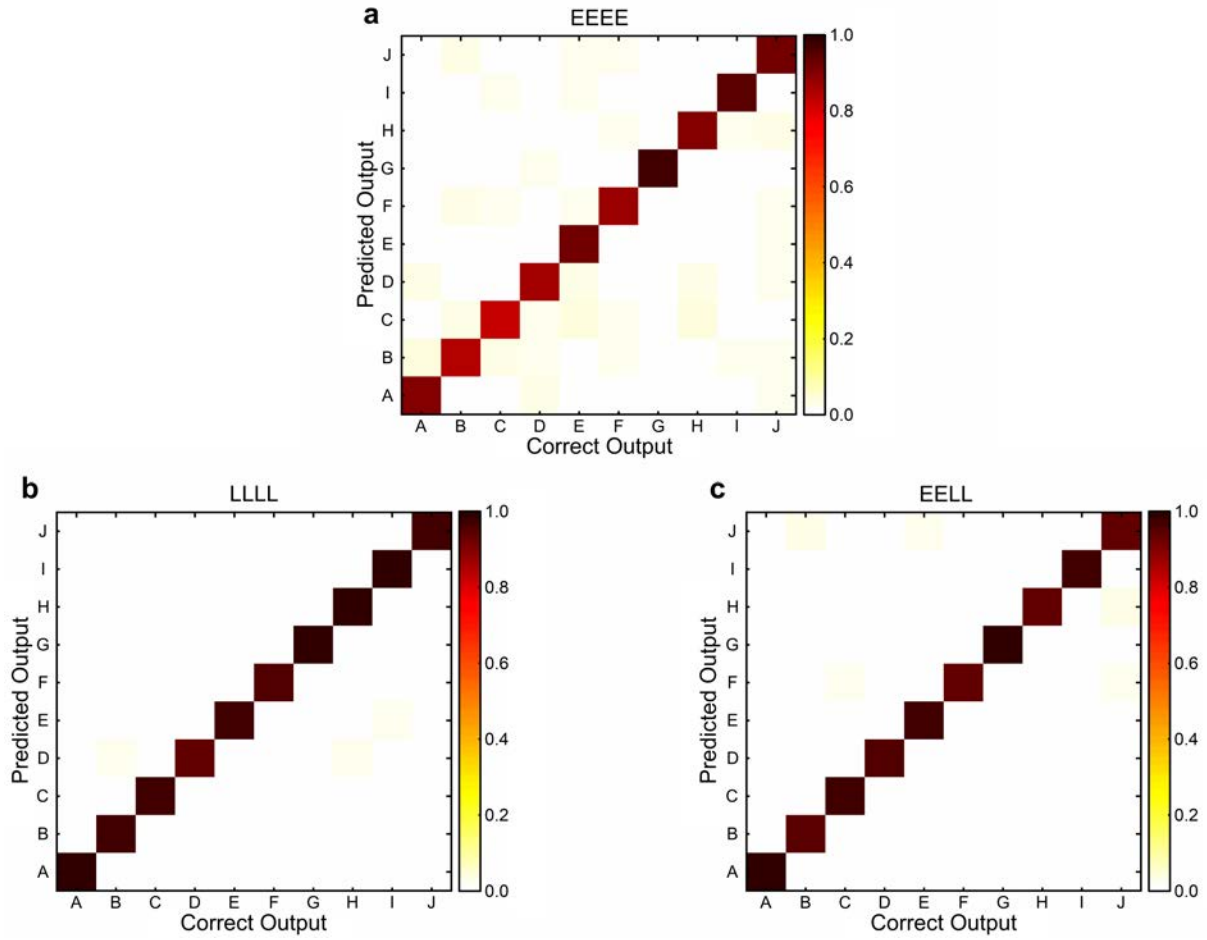
Supplementary Figure 21 | Confusion matrixes of different mixed modes. Experimentally

obtained classification results from the α-In$_2$Se$_3$-based reservoir system working at (**a**) "EEEE",

(**b**) "LLLL" and (**c**) "EELL" modes versus the correct outputs. Recognition rates of 89.5%,

97.7% and 96.3% are achieved respectively. Color bar: occurrence probability of a given

predicted output.
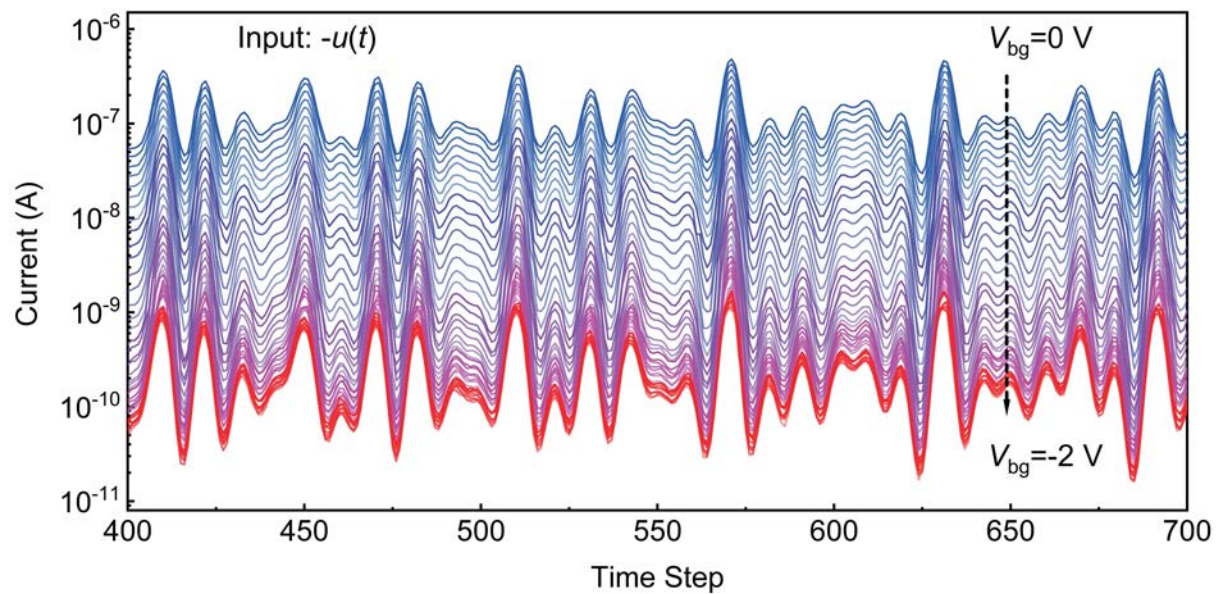
Supplementary Figure 22 | Dynamic current responses when –*u*(*t*) of MSO$_5$ was applied to the α-In$_2$Se$_3$ device with varied back-gate voltages.
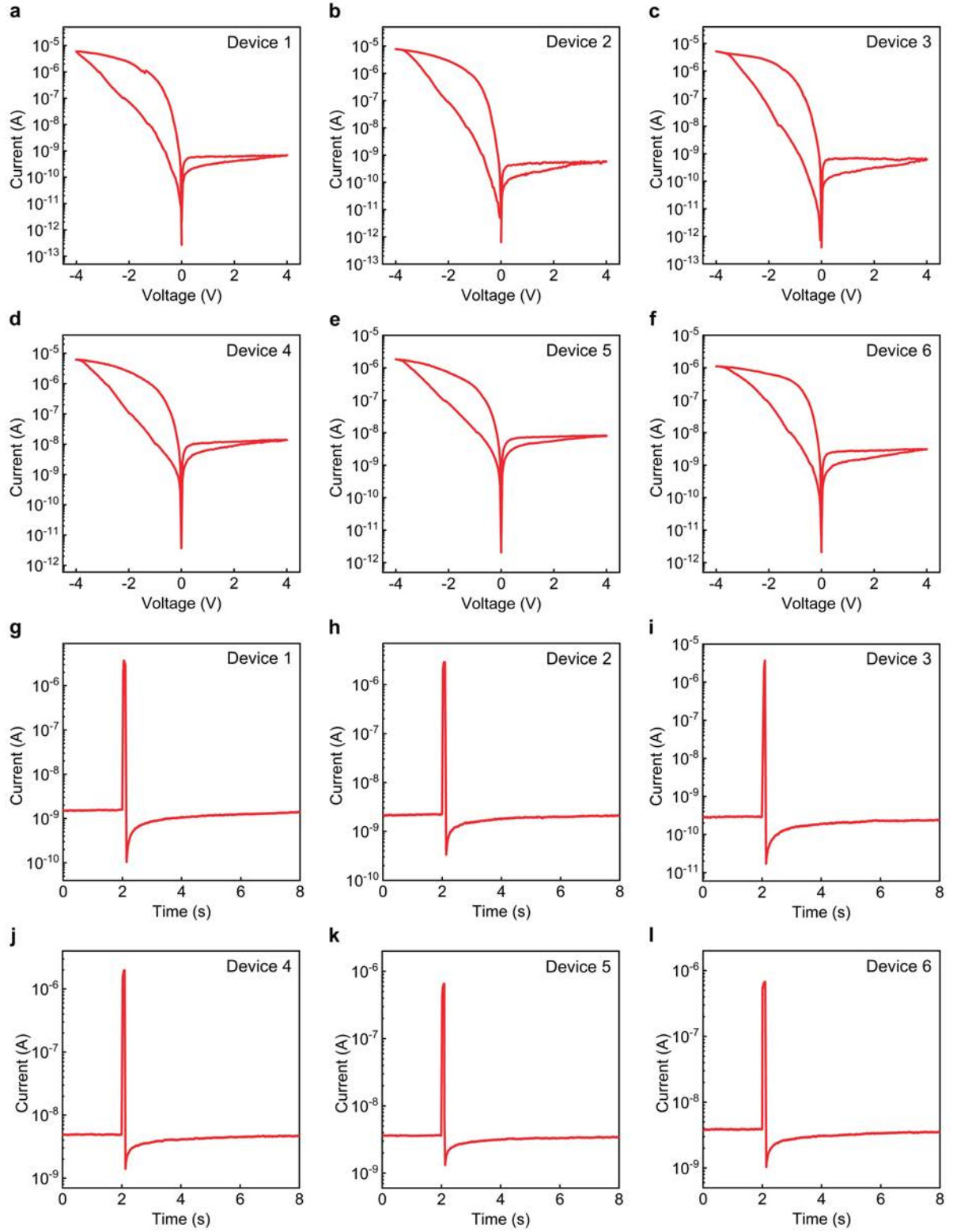
Supplementary Figure 23 | Device-to-device variation of fabricated α-In₂Se₃ devices. (a-f)

DC characteristics of six different α-In₂Se₃ devices (thickness 47 nm, 49 nm, 35 nm, 97 nm,

102 nm and 81 nm). Similar memristive switching curves were observed and thicker devices

exhibit slightly higher current levels. **(g-l)** Transient behavior of six different α-In₂Se₃ devices when an electrical pulse was applied (-2 V, 100 ms) with -0.1 V bias, which exhibit qualitatively similar behavior.

Supplementary Note 1. Transport property of α-In₂Se₃ memristor.

The device can be modeled as a series resistance connecting two back-to-back Schottky junctions, which is dominated by the reverse-biased terminal. The charge transport process can be described by thermionic emission process[S6]

$$I = AA^*T^2 \exp\left(\frac{-q\Phi_{BE}}{kT}\right)\left[\exp\left(\frac{qV}{kT}\right) - 1\right] \tag{1}$$

the reverse-biased current

$$I = AA^*T^2 \exp\left(\frac{-q\Phi_{BE}}{kT}\right) \tag{2}$$

and

$$\Phi_{BE} = \Phi_{B0} - \Delta\Phi \tag{3}$$

$$\Delta\Phi = \sqrt{\frac{q\xi_m}{4\pi\varepsilon_S}} \tag{4}$$

$$\xi_m = \sqrt{\frac{2qN_D}{\varepsilon_S}\left(V + \Phi_{Bi} - \frac{kT}{q}\right)} \tag{5}$$

where A is the area of Schottky barrier, A^* is the effective Richardson constant, q is the electron charge, k is the Boltzmann constant, T is temperature, Φ_{B0} is the ideal barrier height, $\Delta\Phi$ is the barrier lowering induced by image force, Φ_{BE} is the effective barrier height, ξ_m is the maximum electric field, ε_s is the dielectric constant, N_D is the donor impurity density and Φ_{Bi} is the built-in potential. According to these formulas above, a linear relationship is expected between $\ln(I)$ and $V^{1/4}$. As shown in Supplementary Fig. 5a-b, good linear fittings are presented in both SET and RESET process, consistence with the thermionic emission process.

Supplementary Note 2. A comparison between ferroelectric CuInP$_2$S$_6$, MoTe$_2$ and α-In$_2$Se$_3$ for device applications.

CuInP$_2$S$_6$ (CIPS) is a ferroelectric insulator, whose ferroelectricity exists in bulk and few-layer CIPS down to bilayer thickness[S7]. CIPS has been explored as ferroelectric capacitors, and the temperature dependent remnant polarization tests suggested a ferroelectric Curie point at ~315 K[S8]. FeFET[S8] and negative capacitance field-effect transistor (NCFET)[S9] have been demonstrated using CIPS as ferroelectric insulator and MoS$_2$ as channel material. Ferroelectric tunnel junctions (FTJ) with high tunneling electroresistance above 10^7 were fabricated using CIPS as the ferroelectric barrier, and graphene and chromium as contacts[S10]. Therefore, CIPS-based devices have shown potential in nonvolatile memory and logic applications, whereas the low Curie point of CIPS may bring about high temperature stability concerns.

Besides, ferroelectricity of MoTe$_2$ arises from its distorted 1T (d1T) phase, which exhibited out-of-plane ferroelectricity down to monolayer limit[S11]. The d1T-MoTe$_2$ can be obtained by laser processed 2H-MoTe$_2$. FTJ devices based on d1T-MoTe$_2$ and Pt (or graphene) were fabricated with on/off ratio of ~10^3. Notably, the Curie temperature is ~340 K for monolayer d1T-MoTe$_2$ and decreases with increased layer number, which is above room temperature for d1T-MoTe$_2$ below 16 layers. Therefore, d1T-MoTe$_2$ exhibits potential in nonvolatile memory applications, but the material acquisition and thickness dependent Curie temperature may bring about limitations.

In contrast, α-In$_2$Se$_3$ is a ferroelectric semiconductor exhibiting in-plane and out-of-plane ferroelectricity down to monolayer limit[S12-S14], with dipole locking effect[S1,S15]. α-In$_2$Se$_3$

possesses a relatively high Curie temperature, and PFM phase and amplitude loops can be obtained up to 470 K[S16], which is significantly higher than $CuInP_2S_6$ and $MoTe_2$. The existence of in-plane and out-of-plane ferroelectricity facilitates lateral and vertical FSJs[S5,S17,S18]. The dipole locking effect makes it potentially possible to control vertical (horizontal) polarization using horizontal (vertical) electric field[S2,S5,S19]. FeSFETs has been fabricated based on α-In_2Se_3 for memory and synaptic applications[S20-S22], and synaptic devices based on α-In_2Se_3 exhibited coexistence of both long-term and short-term memory effects, which are suitable for implantation of reservoir computing algorithm. Moreover, the dynamic optical response[S23] of α-In_2Se_3 further facilitates in-sensor reservoir computing applications.

Supplementary Note 3. A comparison of reservoir computing and single-valued network on QR code recognition task.

A single-valued system was employed for comparison, using the first point of the 4-pixel as input, which can be seen as a hand-crafted filter [1,0,0,0]. The readout layer is a 200×10 network with ten output neurons (sigmoid activation function), the size of which is kept the same as the readout layer for reservoir computing. The classification accuracy of this network is 97.9%. In comparison, the mode "EEEL" with 98.6% accuracy outperforms the single-valued network, demonstrating that fading memory and nonlinear transformation carried out by the reservoir helped with solving the problem. Meanwhile, the modes "EELL" with 96.3% and "LLLL" with 97.7% accuracies are very close to the accuracy of single-valued network. Mode "LLLL" did not exhibit a higher accuracy, however, it has the advantage for realizing in-sensor reservoir computing. Mode "EEEE" with 89.5% accuracy is much lower than the

accuracy of single-valued network, which indicates the nonlinearity induced by mode "EEEE" actually deteriorates solution of this problem. The above results show that the generated various nonlinear transformation modes may have different effects on solving a certain problem, where some nonlinearities are beneficial whereas some can be harmful. Therefore, the ability of conveniently tuning nonlinear transformation modes and adapting the most suitable nonlinearity to different tasks is very important.

Supplementary References

S1.   Xiao, J. et al. Intrinsic two-dimensional ferroelectricity with dipole locking. *Phys. Rev. Lett.* **120**, 227601 (2018).

S2.   Li, Y. et al. Orthogonal electric control of the out-of-plane field-effect in 2D ferroelectric α-In_2Se_3. *Adv. Electron. Mater.* **6**, 2000061 (2020).

S3.   Liu, L. et al. Atomicaily Resolving Polymorphs and Crystal Structures of In2Se3. *Chem. Mater.* **31**, 10143-10149 (2019).

S4.   Xue, F. et al. Multidirection Piezoelectricity in Mono- and Multilayered Hexagonal alpha-In2Se3. *ACS Nano* **12**, 4976-4983 (2018).

S5.   Xue, F. et al. Gate-tunable and multidirection-switchable memristive phenomena in a van der Waals ferroelectric. *Adv. Mater.* **31**, 1901300 (2019).

S6.   Sze, S. M. & Ng, K. K. *Physics of Semiconductor Devices*. (John Wiley & Sons, Hoboken, NJ, USA, 2006).

S7.   Liu, F. et al. Room-temperature ferroelectricity in $CuInP_2S_6$ ultrathin flakes. *Nat. Commun.* **7**, 12357 (2016).

S8.   Si, M., Liao, P.-Y., Qiu, G., Duan, Y. & Ye, P. D. Ferroelectric Field-Effect Transistors Based on MoS2 and CuInP2S6 Two-Dimensional van der Waals Heterostructure. *ACS Nano* **12**, 6700-6705 (2018).

S9.   Wang, X. et al. Van der Waals negative capacitance transistors. *Nat. Commun.* **10** (2019).

S10.   Wu, J. et al. High tunnelling electroresistance in a ferroelectric van der Waals heterojunction via giant barrier height modulation. *Nat. Electron.* **3**, 466-472 (2020).

S11.   Yuan, S. et al. Room-temperature ferroelectricity in $MoTe_2$ down to the atomic monolayer limit. *Nat. Commun.* **10**, 1775 (2019).

S12.   Ding, W. et al. Prediction of intrinsic two-dimensional ferroelectrics in In_2Se_3 and other III_2-VI_3 van der Waals materials. *Nat. Commun.* **8**, 14956 (2017).

S13.   Zhou, Y. et al. Out-of-plane piezoelectricity and ferroelectricity in layered α-In_2Se_3 nanoflakes. *Nano Lett.* **17**, 5508-5513 (2017).

S14.   Xue, F. et al. Room-temperature ferroelectricity in hexagonally layered α-In_2Se_3 nanoflakes down to the monolayer limit. *Adv. Funct. Mater.* **28**, 1803738 (2018).

S15.   Cui, C. et al. Intercorrelated in-plane and out-of-plane ferroelectricity in ultrathin two-dimensional layered semiconductor In_2Se_3. *Nano Lett.* **18**, 1253-1258 (2018).

S16.   Tang, W. et al. A van der Waals Ferroelectric Tunnel Junction for Ultrahigh-Temperature Operation Memory. *Small Methods* **6** (2022).

S17.   Gabel, M. & Gu, Y. Understanding microscopic operating mechanisms of a van der Waals planar ferroelectric memristor. *Adv. Funct. Mater.* **31**, 2009999 (2021).

S18.   Si, M. et al. Asymmetric Metal/α-In_2Se_3/Si crossbar ferroelectric semiconductor junction. *ACS Nano* **15**, 5689-5695 (2021).

S19.   Dai, M. et al. Intrinsic dipole coupling in 2D van der Waals ferroelectrics for gate-controlled switchable rectifier. *Adv. Electron. Mater.* **6**, 1900975 (2020).

S20.   Si, M. W. et al. A ferroelectric semiconductor field-effect transistor. *Nat. Electron.* **2**, 580-586 (2019).

S21.   Wang, S. et al. Two-dimensional ferroelectric channel transistors integrating ultra-fast memory and neural computing. *Nat. Commun.* **12**, 53 (2021).

S22.   Wang, L. et al. Exploring ferroelectric switching in α-In_2Se_3 for neuromorphic computing. *Adv. Funct. Mater.* **30**, 2004609 (2020).

S23.   Island, J. O., Blanter, S. I., Buscema, M., van der Zant, H. S. & Castellanos-Gomez, A. Gate controlled photocurrent generation mechanisms in high-gain In_2Se_3 Phototransistors. *Nano Lett.* **15**, 7853-7858 (2015).